Journal of Alloys and Compounds 508 (2010) 587–591

Contents lists available at ScienceDirect

Journal of Alloys and Compounds

journal homepage: www.elsevier.com/locate/jallcom

Antibacterial and photocatalytic activities of sonochemically prepared ZnO and Ag–ZnO

C. Karunakaran*, V. Rajeswari, P. Gomathisankar

Department of Chemistry, Annamalai University, Annamalainagar 608002, Tamilnadu, India

ARTICLE INFO

Article history:
Received 12 July 2010
Received in revised form 15 August 2010
Accepted 25 August 2010
Available online 25 September 2010

Keywords:
Semiconductors
Chemical synthesis
Catalysis
Luminescence

ABSTRACT

ZnO and Ag–ZnO (0.5 at.%) nanocrystals have been prepared by sonochemical method and characterized by X-ray diffraction, energy dispersive X-ray analysis, scanning electron micrographs, UV–visible diffuse reflectance spectra, photoluminescence spectra, and impedance spectra. Ag-doping sharpens the band gap absorption, enhances the visible emission and increases the charge transfer resistance. The synthesized ZnO photocatalytically detoxifies cyanide in alkaline medium. The bactericidal activities of the prepared oxides, tested with *Escherichia coli*, are larger than that of commercial ZnO nanoparticles (Sigma–Aldrich). While the antibacterial efficiencies of the prepared ZnO and Ag–ZnO do not differ significantly, their photocatalytic activities to degrade dyes, tested with methyl orange, rhodamine B, and methylene blue, could not be generalized; photocatalysis is also substrate specific. Further, agglomeration of the nanoparticles in dye solution may lead to such results.

1. Introduction

Zinc oxide is a promising material with extensive application in semiconducting, piezoelectric, and gas sensing devices, and in medical use, due to its unique properties and aesthetic morphologies [1]. It has a wide direct band gap (3.37 eV) and a large exciton binding energy (60 meV). Its high chemical stability and low toxicity make it suitable for UV screening applications. Nanoparticulate ZnO is a bactericide and inhibits both Gram-positive and Gram-negative bacteria [2]. It is a photocatalyst as well [3] and its photocatalytic activity is comparable to that of TiO_2. It shows *n*-type conductivity, because of its native defects such as zinc interstitials and oxygen vacancies. Ag-doping is found to be effective for the fabrication of *p*-type ZnO. Doping ZnO with Ag modifies the optical and electronic properties of the oxide, which in turn influence the photocatalytic activity [4–6]. Photocatalysis occurs on the surface of semiconductor and the photocatalytic activity strongly depends on the morphology and surface modification of the oxide [7,8]. Shining semiconductor nanocrystals with light of energy not less than the band gap creates electron-hole pairs, electrons in the conduction band (CB) and holes in the valence band (VB) [9]. Some of these pairs diffuse to the crystal surface and react with the adsorbed substrates leading to photocatalysis. The hole oxidizes the organics. The adsorbed oxygen molecule picks up the electron and transforms into highly active superoxide radical ($O_2^{\bullet -}$). In presence of moisture, $O_2^{\bullet -}$ produces reactive species like $HO^{\bullet}$, $HO_2^{\bullet}$, and H_2O_2, which act as oxidants. Hole-trapping by either the surface hydroxyl groups or the adsorbed water molecules generates short-lived $HO^{\bullet}$ radicals. Here we present the sonochemical preparation of nanocrystalline ZnO and Ag–ZnO; both the oxides show large antimicrobial activity than the commercial ZnO nanoparticles (Sigma–Aldrich). Regarding the photocatalytic activities of the prepared ZnO and Ag–ZnO to degrade dyes, contrary to many reports of enhanced dye-degradation by Ag–ZnO, the present results are mixed. With methylene blue, rhodamine B, and methyl orange as test substrates, the observed photocatalytic activity is found to be substrate specific also. Preparation of Ag–ZnO nanoparticles by chemical [10], photochemical [11,12], coprecipitation [5,13], sol–gel [4], hydrothermal [14–18] or solvothermal [19], microwave [20], flame spray pyrolysis [21], electrospinning [22], and RF magnetron sputtering [23] methods and hybrid induction and laser heating technique [24] have been reported already. Although reports on synthesis of nanocrystalline ZnO are numerous, ZnO nanostructure continues to be of interest; it has been synthesized in the form of nanoparticles by chemical precipitation [25], nanowires by solution-phase reaction [26], nanoparticles, nanosheets, and hexagonal nanopyramids by direct calcination [27], and nanoparticles, nanowires, nanobelts, nanorods, prismatic nanorods, nanosheets, nanoflowers, nanospheres, and hollow spheres by hydrothermal method recently [28–32].

* Corresponding author. Tel.: +91 9443481590; fax: +91 4144238145.
E-mail address: karunakaranc@rediffmail.com (C. Karunakaran).

0925-8388/$ – see front matter © 2010 Elsevier B.V. All rights reserved.
doi:10.1016/j.jallcom.2010.08.128

2. Experimental details

2.1. Sonochemical preparation

All the chemicals used were of analytical grade. Deionized distilled water was employed throughout experiments. Zinc acetate (2.195 g) and cetyltrimethylammonium bromide, CTAB (0.034 g), without or with silver nitrate (0.0084 g), were dissolved in water (100 mL) and sonicated (37 ± 3 kHz, 100 W) for 1 h. Continuing sonication, NaOH (0.2 M, 50 mL) was added gradually to the solution and precipitation occurred immediately; the pH turned to 9.5. It was kept aside for a day and the precipitate was dried under vacuum and calcined at 500 °C for 2 h in a muffle furnace fitted with a PID temperature controller. The heating rate was set at 10 °C min^{-1}.

2.2. Characterization

The powder X-ray diffraction (XRD) patterns of the oxides were recorded using Cu Kα rays at 1.5406 Å with a PANalytical X'Pert PRO diffractometer in a 2θ range of 10–70° with a scan rate of 0.05° s^{-1} at 40 kV and 30 mA. The morphologies of the oxides were determined using a JEOL JSM-5610 scanning electron microscope (SEM) equipped with BE detector. The samples were placed on an adhesive carbon slice supported on copper stubs and coated with 10 nm thick gold using JEOL JFC-1600 auto fine coater before measurement. JEOL JSM-5610 SEM equipped with EDX was also used to record the energy dispersive X-ray (EDX) spectrum. The UV–visible diffuse reflectance spectra of the oxides were recorded using a PerkinElmer Lamda 35 spectrometer. A PerkinElmer LS 55 fluorescence spectrometer was employed to record the photoluminescence (PL) spectra of the oxides at room temperature. The nanoparticles were dispersed in carbon tetrachloride and were excited at 340 nm. A CH Instrument Electrochemical Analyzer 604C was used to obtain the impedance spectra (IS) at room temperature in air over the frequency range of 1 MHz to 1 Hz. The disk area was 0.5024 cm^2 and the thicknesses of ZnO and 0.5% Ag–ZnO pellets were 0.70 and 0.85 mm, respectively.

2.3. Photocatalytic study

A photoreactor fitted with 8 W mercury lamps of wavelength 365 nm (Sankyo Denki, Japan) and highly polished anodized aluminum reflector was employed for the photodegradation experiments. Borosilicate glass tube of 15 mm inner diameter was used as the reaction vessel. It was placed at the center of the reactor. The reactor was fitted with cooling fans at the bottom to dissipate the generated heat. The solution was illuminated with four lamps mutually set at right angle. The photon flux (I) of the UV light was determined by ferrioxalate actinometry.

Solutions of the dyes of required concentrations were prepared afresh and used. After the addition of the oxide (0.020 g) to the dye solution (25 mL), air was purged through the solution, which kept the oxide particles under suspension and at constant motion. After the illumination, the oxide was removed by centrifugation and the undegraded dyes were spectrophotometrically estimated, after proper dilution. The absorptions of methyl orange, rhodamine B, and methylene blue in the visible light at 464, 555, and 663 nm, respectively, were used for the analysis; calibration curve for each dye was constructed by recording its absorbance at different ppm. For the photocatalytic oxidation of cyanide ion, freshly prepared alkaline KCN solution (pH 12.5) was used and the procedure followed was the same as that of dye degradation; the cyanide ion was analyzed spectrophotometrically at 590 nm, by complexing it with ninhydrin in alkaline medium [33].

2.4. Bactericidal study

A nutrient broth culture medium of pH 7.4 was prepared by dissolving 13.0 g nutrient broth (5.0 g peptone, 5.0 g NaCl, 2.0 g yeast extract, 1.0 g beef extract) in 1 L distilled water followed by sterilization in an autoclave at 121 °C. MacConkey agar plates were prepared separately by dissolving 55 g MacConkey agar (20 g peptic digest of animal tissue, 10 g lactose, 5 g sodium taurocholate, 0.04 g neutral red, 20 g agar) in 1 L boiling distilled water followed by sterilization in an autoclave at 121 °C and poured into Petri dish. *Escherichia coli* bacteria were inoculated in 10 mL of a nutrient broth and incubated for 24 h at 37 °C. The cultured bacteria were centrifuged at 3500 rpm for 5 min, washed twice with an autoclaved NaCl (0.9%) solution and suspended in 50 mL of an autoclaved 0.9% NaCl solution. For the counting of *E. coli* colonies in CFU mL^{-1}, the bacterial solution was successively diluted to 10^9 times using 0.9% NaCl solution in order to achieve about 100–125 colonies on the Petri dish. 10 μL of the diluted *E. coli* was streaked on the MacConkey agar plate using a loop and incubated at 37 °C for 24 h. The CFU was counted by a viable count method.

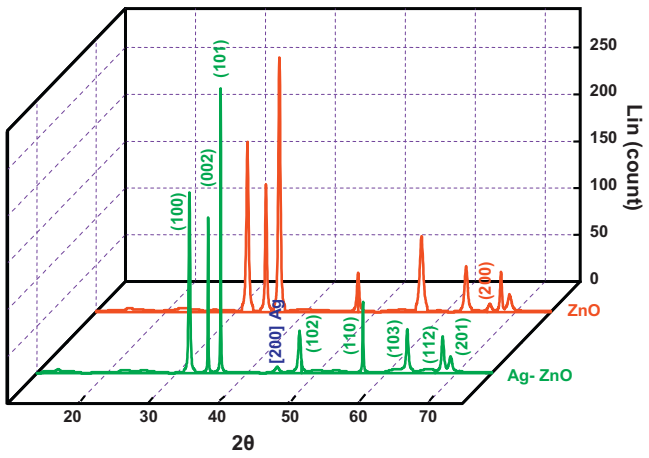

Fig. 1. X-ray diffraction patterns of ZnO and Ag–ZnO.

To *E. coli* solution (25 mL) taken in a bottle, the oxide (20 mg) was added and shaken well continuously without any illumination. At the required time intervals, a finite volume of *E. coli* solution was removed from the oxide, diluted stepwise and enumerated as stated already.

3. Results and discussion

3.1. Crystal structure

The XRDs of sonochemically prepared Ag–ZnO and ZnO are displayed in Fig. 1. They show the crystal structures of the doped as well as the undoped oxides as primitive hexagonal with crystal constants a and b as 3.249 Å and c as 5.205 Å. The diffraction patterns match with the standard JCPDS pattern of zincite (89–7102). Ag can be incorporated in ZnO lattice as a substituent for Zn^{2+} or as an interstitial atom [8]. If silver were substituted for Zn^{2+}, a corresponding peak shift should have been observed in the XRD. Absence of such shifts in the recorded XRD suggests the segregation of Ag particles in the grain boundaries of ZnO. Otherwise, only an insignificant quantity of Ag would have gone to the substitutional Zn site. However, the latter possibility is less likely because of the difference in ionic radii between Zn^{2+} (0.72 Å) and Ag^+ (1.22 Å). The silver particles preferentially choose to segregate around the ZnO grain boundaries. This is supported by the fact that the XRD of doped oxide also displays the 200 peak of face centered cubic phase of metallic Ag at 44.4° (JCPDS 03-092). In the prepared Ag–ZnO, Ag is unlikely to be present as Ag_2O. This is because the prepared doped oxide has been calcined at 500 °C whereas Ag_2O decomposes to Ag at 400 °C. The average crystallite size of the prepared Ag–ZnO and ZnO have been deduced from the half-width of the full maximum (HWFM) of the most intense peaks of the respective crystals using the Scherrer equation, $D = 0.9\lambda/\beta\cos\theta$, where D is the average crystallite size, λ is the X-ray wavelength, θ is the Bragg angle and β is the corrected half-peak width of the experimental sample. The average crystal size of the doped oxide is larger that the undoped one and the results are presented in Table 1. The specific surface areas of the nanoparticles, also given in Table 1, have been deduced using the relationship $S = 6/\rho D$, where S is the surface area and ρ is the material density. The low surface area of Ag–ZnO is due to its

Table 1
Crystal size (D), surface area (S), band gap (E_g), near band gap emission (NBE), deep level emission (DLE), ohmic (R_Ω) and charge transfer (R_{CT}) resistances, specific conductance (σ) and capacitance (C).

Oxide	D (nm)	S (m^2 g^{-1})	E_g (eV)	NBE (nm)	DLE (nm)	R_Ω (kΩ)	R_{CT} (MΩ)	σ (μS m^{-1})	C (pF)
Ag–ZnO	87	12	3.14	415	467	13.0	15.5	1.09	27.7
ZnO	25	44	3.14	410	467	97.4	2.00	6.95	17.3

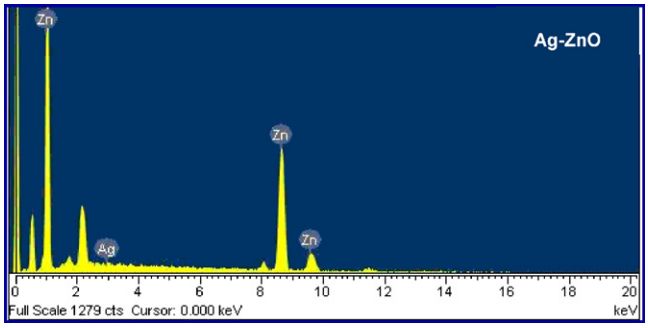

Fig. 2. Energy dispersive X-ray spectrum of Ag–ZnO.

larger crystal size. The energy dispersive X-ray spectroscopic analysis of the doped oxide also confirms the presence of Ag in the doped oxide. Fig. 2 is the EDX spectrum of the doped oxide. The SEMs of Ag–ZnO and ZnO are displayed in Fig. 3. The SEMs reveal that ZnO obtained by sonochemical method is fake-like while Ag–ZnO prepared by the same method is highly agglomerated.

3.2. Optical properties

The diffuse reflectance spectra (DRS) of Ag–ZnO and ZnO are shown in Fig. 4. The reflectance data are reported as $F(R)$ value, obtained by the application of Kubelka–Munk algorithm. The figure displays the transformation of the DRS of ZnO on doping with Ag. The band gap absorption turns sharp on doping ZnO with Ag. The work function of Ag, which lies between the VB and CB of ZnO, may facilitate the light absorption capacity [5]. Table 1 presents the

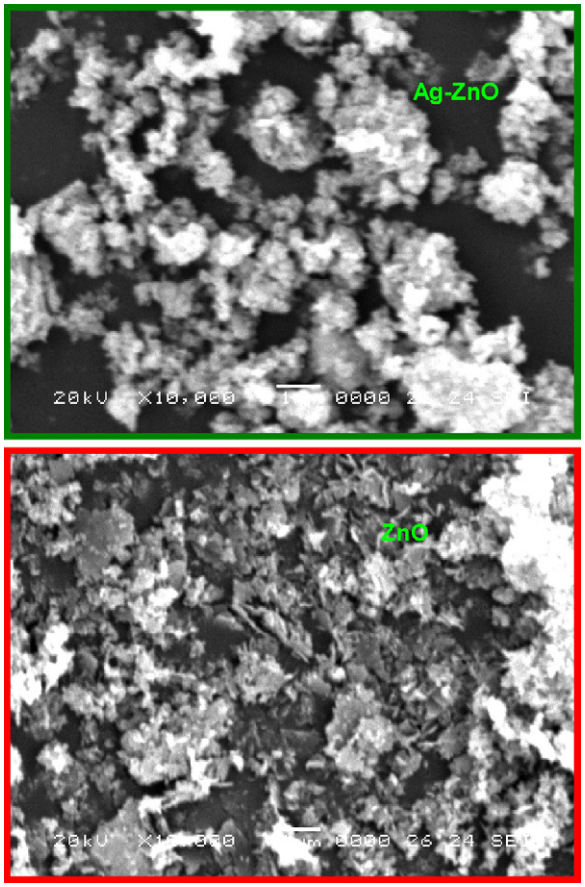

Fig. 3. SEM images of ZnO and Ag–ZnO.

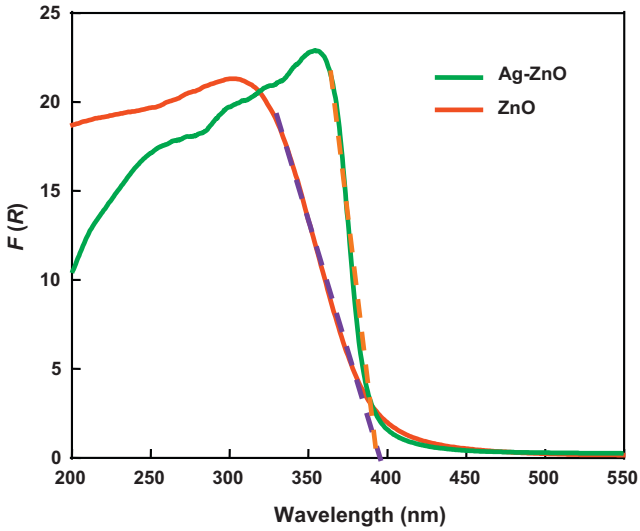

Fig. 4. Diffuse reflectance spectra of ZnO and Ag–ZnO.

deduced band gaps. These values show that Ag-doping does not modify the absorption edge of ZnO. The Gaussian fits of the photoluminescence spectra of ZnO and Ag–ZnO are presented in Fig. 5. Both the oxides display near band gap emission (NBE) because of excitonic recombination [8]. These emissions agree satisfactorily with the band gaps deduced from the Kubelka–Munk plots. The UV and visible emissions of ZnO and Ag–ZnO are listed in Table 1. The blue or deep level emission (DLE) is due to the recombination of electron in singly occupied oxygen vacancy with the photogenerated hole in the VB [8]. Analysis of the NBE and DLE of ZnO and Ag–ZnO reveals enhancement of blue emission on doping ZnO with Ag by sonochemical method. The ratio of intensity of DLE to that of NBE reflects the extent of defect and the ratios for ZnO and Ag–ZnO are 1.4 and 1.9, respectively. That is, the optical defect is more in Ag–ZnO than in ZnO.

3.3. Electrical properties

In nanocrystals, the majority of atoms or ions are present in the grain boundaries or within one or two layers from the boundary. These grain boundaries may contain a high density of defects like vacancies. Defects in semiconductor nanocrystals strongly influence the electrical properties of the materials and the pho-

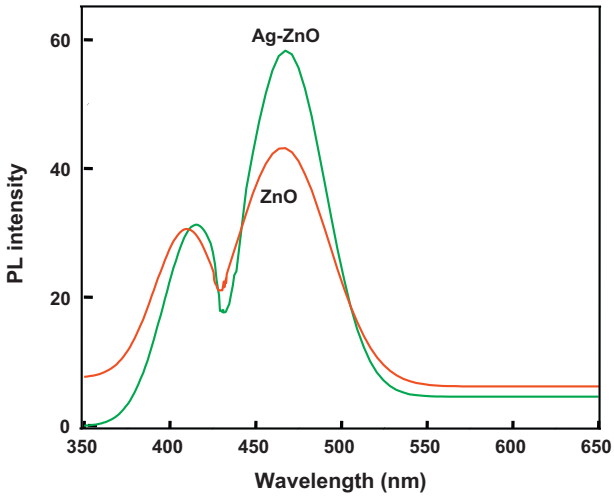

Fig. 5. Photoluminescence spectra of ZnO and Ag–ZnO.

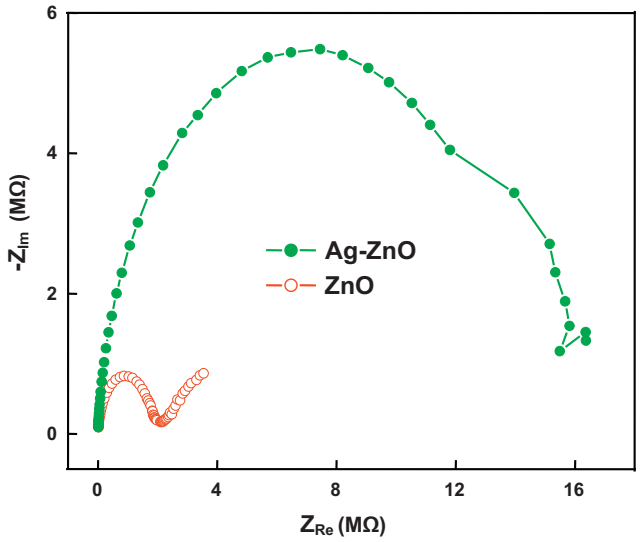

Fig. 6. Nyquist plots of ZnO and Ag–ZnO.

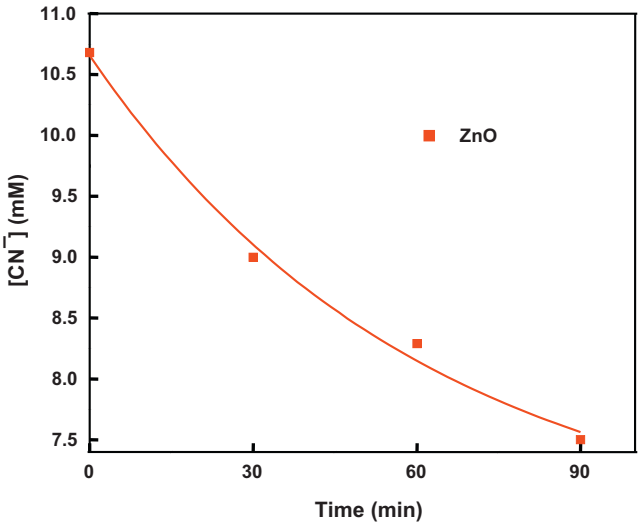

Fig. 7. Time-profile of cyanide photooxidation. 0.025 g ZnO loading, 26.8 mg L^{-1} dissolved O_2, 7.8 mL s^{-1} airflow rate, 12.5 pH, 365 nm, 48.8 μEinstein L^{-1} s^{-1}, 25 mL cyanide.

tocatalytic activity of the semiconductor depends on the extent of defects in the crystals. Impedance spectroscopy (IS) is a relatively new and powerful tool to probe the electrical properties of semiconductors [34]. It could be used to investigate the dynamics of the mobile and bound charges in the interfacial or bulk region of the semiconductors. In polycrystalline materials, the overall sample resistance may be a combination of the intragranular or bulk crystal resistance and intergranular or grain boundary resistance. Generally, the impedance data are analyzed in terms of an equivalent circuit model. An electrode interface undergoing an electrochemical reaction is typically analogous to an electric circuit consisting of a specific combination of capacitors and resistors. By fitting the IS data to a model or an equivalent circuit the electrical properties of the semiconductors could be inferred. The impedance spectra of Ag–ZnO and ZnO show decrease of impedance with increase of frequency indicating the capacitance of the semiconductors prepared. The corresponding Nyquist plots, the popular format of evaluating the impedance data, are presented in Fig. 6. The semicircle in the Nyquist plot is the expected response of the simple circuit. Here, it is relevant to state that Ag_2O/ZnO displays two partially overlapping semicircular arcs [35]. The ohmic or uncompensated resistance (R_Ω) corresponds to the grain boundary or intergranular resistance and the polarization or electron-transfer (charge-transfer) resistance (R_P or R_{CT}) refers to the intragranular or bulk crystal resistance. The R_{CT} is related to the Warburg resistance. It is controlled by the specific conductance, σ. The constant phase element (CPE) may be associated with a non-uniform distribution of current due to material heterogeneity and is equivalent to a double layer capacitance (C). The specific conductance has been deduced from the measured charge-transfer resistance and the capacitance has been obtained using the equations $\omega_{max} = 1/CR_{CT}$ and $\omega_{max} = 2\pi f$, where f is the highest frequency exhibited by the semicircle of the Nyquist plot. The determined ohmic and charge-transfer resistances and capacitances of Ag–ZnO and ZnO are presented in Table 1. The results show that Ag-doping increases the charge transfer resistance as well as the capacitance. The decrease of ohmic resistance on doping ZnO with Ag is in agreement with the results of Kuo et al. [36].

3.4. Photocatalytic activity

Sonochemically synthesized ZnO photocatalyzes cyanide ion oxidation in alkaline medium. The pK_a of HCN is 9.3. Hence to avoid its liberation into the atmosphere the detoxification was done in a highly alkaline solution. Fig. 7 displays the time profile of cyanide photodetoxification. Cyanide ion reacts with Ag and hence Ag–ZnO is unsuitable for the photocatalytic removal of cyanide. The photocatalytic efficiencies of the prepared ZnO and Ag–ZnO have been compared by employing three dyes of different classes and structures. The dyes used are azo dye methyl orange, xanthen dye rhodamine B, and heterocyclic dye methylene blue. The degradation profiles of all the three dyes, photocatalyzed by ZnO and Ag–ZnO, are displayed in Fig. 8; the results are corrected for adsorption. The time profiles show inhibition of photocatalytic degradation of methylene blue and rhodamine B on doping ZnO with Ag by sonochemical method. This is in contrast to the observed enhancement of photodegradation of methyl orange on doping ZnO with Ag by the same method. Further, reports of enhanced photocatalytic activity of Ag-doped ZnO are many [12,17–19,21,22,24]. But, there are also a few reports of inhibition of photocatalytic activity of ZnO on doping with Ag under certain conditions. Ag–ZnO

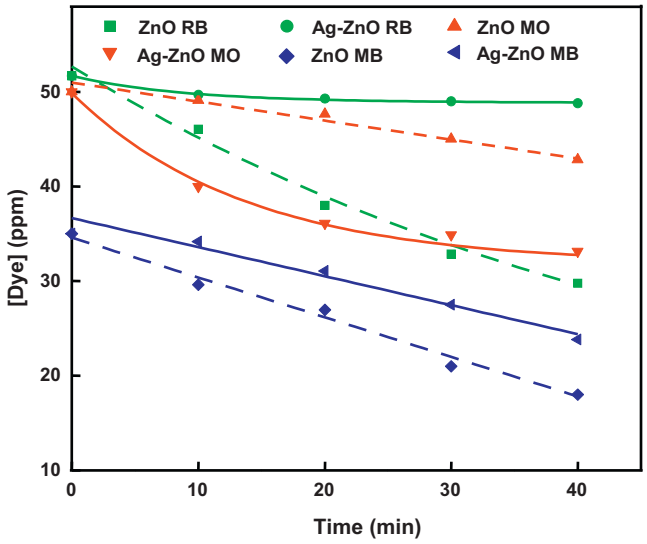

Fig. 8. Temporal profile of dye photodegradation; RB: Rhodamine B; MO: methyl orange; MB: methylene blue. 0.020 g oxide loading, 9.3 mg L^{-1} dissolved O_2, 7.8 mL s^{-1} airflow rate, 5.5 pH, 365 nm, 25.4 μEinstein L^{-1} s^{-1}, 25 mL dye.

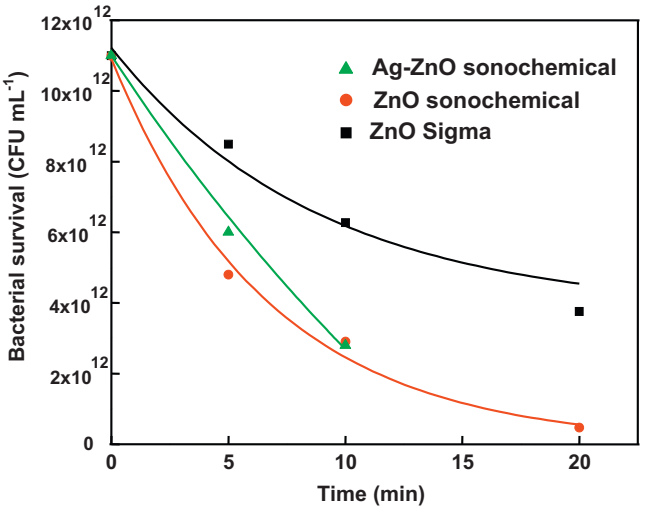

Fig. 9. Temporal profile of *E. coli* disinfection. 0.020 g oxide loading, 7.1 pH, 25 mL *E. coli* solution.

obtained by RF magnetron sputtering exhibits mixed results. While short sputtering time of 1 and 5 s enhance the photocatalytic activity long sputtering time of 30, 60 and 150 s inhibit the same [23]. Similarly, the photocatalytic activity depends on the calcination temperature; Ag–ZnO (1, 3, 5%) calcined at 1000 and 800 °C are less photocatalytically active than ZnO and those calcined at 300, 400, 500 and 600 °C are more photocatalytically active [4]. One of the possible reasons for the observed mixed results of photocatalytic activities is that the photocatalysis is also substrate specific. Further, the nanoparticles agglomerate in dye solution leading to such results.

3.5. Bactericidal activity

The time profiles of *E. coli* disinfection by sonochemically prepared Ag–ZnO and ZnO in aqueous suspension in absence of direct illumination are shown in Fig. 9. The corresponding profile of *E. coli* inactivation by commercial ZnO nanoparticles (Sigma–Aldrich) is appended for comparison. The crystal structure of commercial ZnO, determined by powder XRD (not shown), is also wurtzite; the average crystallite size and surface area are 58 nm and 18 $m^2 g^{-1}$, respectively. In absence of the oxides the *E. coli* population remains unaffected during the experimental period displaying the bactericidal activity of the oxides. *E. coli* bacteria in 0.9% saline were used for the evaluation of the bactericidal activity. The cell population was determined by a viable count method on MacConkey agar plates after proper dilution of the culture. The temporal profiles show the enhanced bactericidal activity of sonochemically prepared oxides. The exponential decrease of *E. coli* population provides the specific rates of *E. coli* inactivation by commercial ZnO nanoparticles and sonochemically prepared ZnO and Ag–ZnO as 0.054, 0.156, and 0.137 s^{-1}, respectively, indicating that the antibacterial activity of sonochemically prepared ZnO is about three times that of commercial ZnO. The mechanism of bacteria inactivation by ZnO [2,37,38] and Ag [39] nanoparticles has been discussed elsewhere and operation of similar mechanism is possible.

4. Conclusions

Nanocrystalline ZnO and Ag–ZnO (0.5 at.%), prepared by sonochemical method, show larger bactericidal activity than commercial ZnO nanoparticles (Sigma–Aldrich). Ag-doping by sonochemical method sharpens the band gap absorption, enhances the visible emission, and increases the charge transfer resistance. The synthesized ZnO photocatalytically detoxifies cyanide in alkaline medium. The antibacterial efficiencies of the prepared ZnO and Ag–ZnO, tested with *E. coli*, do not differ significantly. But, the photocatalytic activities of ZnO and Ag–ZnO to degrade dyes, tested with methylene blue, methyl orange, and rhodamine B, are substrate specific.

Acknowledgements

The authors thank the Council of Scientific and Industrial Research (CSIR), New Delhi, India, for the financial support through research grant no. 01(2031)/06/EMR-II and P.G. is grateful to CSIR for SRF. The authors also thank Dr. J. Jayabharathi, Annamalai University for the DRS and PL facilities.

References

[1] Z.L. Wang, Mater. Sci. Eng. R 64 (2009) 33.
[2] L. Zhang, Y. Ding, M. Povey, D. York, Prog. Nat. Sci. 18 (2008) 939.
[3] J. Das, D. Khushalani, J. Phys. Chem. C 114 (2010) 2544.
[4] R. Georgekutty, M.K. Seery, S.C. Pillai, J. Phys. Chem. C 112 (2008) 13563.
[5] Y. Zheng, C. Chen, Y. Zhan, X. Lin, Q. Zheng, K Wei, J. Zhu, J. Phys. Chem. C 112 (2008) 10773.
[6] M.-K. Lee, T.G. Kim, W. Kim, Y.-M. Sung, J. Phys. Chem. C 112 (2008) 10079.
[7] B. Li, Y. Wang, J. Phys. Chem. C 114 (2010) 890.
[8] T. Sun, J. Qiu, C. Liang, J. Phys. Chem. C 112 (2008) 715.
[9] X. Hu, G. Li, J.C. Yu, Langmuir 26 (2010) 3031.
[10] J.Z. Wu, J.P. Tu, Y.F. Yuan, M. Ma, X.L. Wang, L. Zhang, R.L. Li, J. Zhang, J. Alloys Compd. 479 (2009) 624.
[11] T. Alammar, A.-V. Mudring, J. Mater. Sci. 44 (2009) 3218.
[12] J. Liqiang, W. Dejun, W. Baiqi, L. Shudan, X. Baifu, F. Honggang, S. Jiazhong, J. Mol. Catal. A 244 (2006) 193.
[13] G. Zhou, J. Deng, Mater. Sci. Semicond. Process. 10 (2007) 90.
[14] S. Baruah, J. Dutta, Sci. Technol. Adv. Mater. 10 (2010) 013001.
[15] W. Lu, S. Gao, J. Wang, J. Phys. Chem. C 112 (2008) 16792.
[16] X.-Y. Ye, Y.-M. Zhou, Y.-Q. Sun, J. Chen, Z.-Q. Wang, J. Nanopart. Res. 11 (2009) 1159.
[17] Y. Zhang, J. Mu, J. Colloid Interface Sci. 309 (2007) 478.
[18] J. Xu, Y. Chang, Y. Zhang, S. Ma, Y. Qu, C. Xu, Appl. Surf. Sci. 255 (2008) 1996.
[19] Y. Zheng, L. Zheng, Y. Zhan, X. Lin, Q. Zheng, K. Wei, Inorg. Chem. 46 (2007) 6980.
[20] S. Bhattacharyya, A. Gedanken, J. Phys. Chem. C 112 (2008) 659.
[21] M.J. Height, S.E. Pratsinis, O. Mekasuwandumrong, P. Praserthdam, Appl. Catal. B 63 (2006) 305.
[22] D. Lin, H. Wu, R. Zhang, W. Pan, Chem. Mater. 21 (2009) 3479.
[23] T. Tan, Y. Li, Y. Liu, B. Wang, X. Song, E. Li, H. Wang, H. Yan, Mater. Chem. Phys. 111 (2008) 305.
[24] R. Wang, J.H. Xin, Y. Yang, H. Liu, L. Xu, J. Hu, Appl. Surf. Sci. 227 (2004) 312.
[25] J. Yang, X. Liu, L. Yang, Y. Wang, Y. Zhang, J. Lang, M. Gao, B. Feng, J. Alloys Compd. 477 (2009) 632.
[26] P.-C. Kao, S.-Y. Chu, B.-J. Li, J.-W. Chang, H.-H. Huang, Y.-C. Fang, R.-C. Chang, J. Alloys Compd. 467 (2009) 342.
[27] G. Guo, C. Shi, D. Tao, W. Qian, D. Han, J. Alloys Compd. 472 (2009) 343.
[28] R.M. Trommer, A.K. Alves, C.P. Bergmann, J. Alloys Compd. 491 (2010) 296.
[29] P. Huang, X. Zhang, J. Wei, B. Feng, J. Alloys Compd. 489 (2010) 614.
[30] M.S. Mohajerani, A. Lak,. Simchi, J. Alloys Compd. 485 (2009) 616.
[31] C.-H. Lu, Y.-C. Lai, R.B. Kale, J. Alloys Compd. 477 (2009) 523.
[32] M. Mazloumi, S. Taghavi, H. Arami, S. Zanganesh, A. Kajbafvala, M.R. Shayegh, S.K. Sadrnezhaad, J. Alloys Compd. 468 (2009) 303.
[33] P. Nagaraja, M.S. Hemanthakumar, H.S. Yathirajan, J.S. Prakash, Anal. Sci. 18 (2002) 1027.
[34] E. Barsoukov, J.R. Macdonald, Impedance Spectroscopy. Theory, Experiment and Application, Wiley-Interscience, New Jersey, 2005.
[35] J. Jose, M.A. Khadar, Acta Mater. 49 (2001) 729.
[36] S.-T. Kuo, W.-H. Tuan, J. Shieh, S.-F. Wang, J. Eur. Ceram. Soc. 27 (2007) 4521.
[37] W. Jiang, H. Mashayekhi, B. Xing, Environ. Pollut. 157 (2009) 1619.
[38] X. Hu, S. Cook, P. Wang, H.-M. Hwang, Sci. Total Environ. 407 (2009) 3070.
[39] V.K. Sharma, R.A. Yngard, Y. Lin, Adv. Colloid Interface Sci. 145 (2009) 83.